

**Titre:** The structural amphiphilicity of cellulose nanocrystals characterized from their cohesion parameters  
Title: from their cohesion parameters

**Auteurs:** Charles Bruel, Jason Robert Tavares, Pierre Carreau, & Marie-Claude Heuzey  
Authors: Heuzey

**Date:** 2019

**Type:** Article de revue / Article

**Référence:** Bruel, C., Tavares, J. R., Carreau, P., & Heuzey, M.-C. (2019). The structural amphiphilicity of cellulose nanocrystals characterized from their cohesion parameters. *Carbohydrate Polymers*, 205, 184-191.  
**Citation:** <https://doi.org/10.1016/j.carbpol.2018.10.026>

## Document en libre accès dans PolyPublie

Open Access document in PolyPublie

**URL de PolyPublie:** <https://publications.polymtl.ca/4111/>  
PolyPublie URL:

**Version:** Version finale avant publication / Accepted version  
Révisé par les pairs / Refereed

**Conditions d'utilisation:** CC BY-NC-ND  
Terms of Use:

## Document publié chez l'éditeur officiel

Document issued by the official publisher

**Titre de la revue:** Carbohydrate Polymers (vol. 205)  
Journal Title:

**Maison d'édition:** Elsevier  
Publisher:

**URL officiel:** <https://doi.org/10.1016/j.carbpol.2018.10.026>  
Official URL:

**Mention légale:** © 2019. This is the author's version of an article that appeared in Carbohydrate Polymers (vol. 205) . The final published version is available at <https://doi.org/10.1016/j.carbpol.2018.10.026>. This manuscript version is made available under the CC-BY-NC-ND 4.0 license <https://creativecommons.org/licenses/by-nd/4.0/>  
Legal notice:

# The structural amphiphilicity of cellulose nanocrystals characterized from their cohesion parameters

Charles Bruel<sup>1</sup>, Jason R. Tavares, Pierre J. Carreau, Marie-Claude Heuzey<sup>2</sup>

Research Center for High Performance Polymer and Composite Systems (CREPEC),  
Chemical Engineering Department, Polytechnique Montreal, P.O. Box 6079, Stn  
Centre-Ville, Montreal, QC H3C 3A7, Canada.

---

## Abstract

Cellulose nanocrystals (CNCs), usually considered as isotropically polar nanoparticles, are sheet-like crystalline assemblies of cellulose chains. Here, we link the anisotropy of the CNC structure to an amphiphilic behavior in suspension. The Hansen solubility parameters (HSP:  $\delta_D$ ;  $\rho$ ;  $\chi_H$ ) of wood-based  $H_2SO_4$ -hydrolyzed CNCs were measured from sedimentation tests in a wide set of 59 solvents and binary mixtures. Two sets of cohesion parameters corresponding to a polar surface (18.1; 20.4; 15.3) (0.5; 0.5; 0.4) MPa<sup>1/2</sup> and to a mildly non-polar one (17.4; 4.8; 6.5) (0.3; 0.5; 0.6) MPa<sup>1/2</sup> were determined, with respective solubility radii of 7.8 and 2.1 MPa<sup>1/2</sup>. The polar sphere is thought to correspond to the (110)&(1̄1̄0) surfaces of cellulose I nanocrystals, while the smaller non-polar sphere is coherent with the exposure of (200) surfaces. The HSP graph provides new insights on the amphiphilic nature of CNCs and **a mapping of their chemical affinity for solvents and polymer matrices**.

*Keywords:*

cellulose nanocrystals, surface properties, structure-property relationships, **chemical affinity**, amphiphilicity, Hansen solubility parameters

---

<sup>1</sup>charles.bruel@polymtl.ca

<sup>2</sup>marie-claude.heuzey@polymtl.ca

<sup>1</sup> 1. Introduction

<sup>2</sup> D-glucopyranose polymerization produces, through a dehydration, polysac-  
<sup>3</sup> charides such as starch, glycogen, dextran, and cellulose (Dufresne, 2017;  
<sup>4</sup> French, 2017). In (1,4)-linked macromolecules, anhydroglucose rings are  
<sup>5</sup> locked in a chair conformation where all their hydrophilic hydroxyl groups  
<sup>6</sup> are in equatorial position while all their more hydrophobic C-H bonds are  
<sup>7</sup> axial. For -(1,4)-linked polysaccharides, such as dextrins, it results in an  
<sup>8</sup> apolar behavior in solution (Dufresne, 2017), a feature famously exploited  
<sup>9</sup> in cyclodextrins whose structure forms a cavity rich in C-H bonds that may  
<sup>10</sup> be used to encapsulate hydrophobic chemicals (Marques, 2010), including for  
<sup>11</sup> delivery in living organisms (Chaturvedi et al., 2011).

<sup>12</sup> Although being insoluble in water, amorphous cellulose,  $\alpha$ -(1,4)-linked  
<sup>13</sup> polymer of anhydroglucopyranose (Fig. 1.a&b), does not display such a  
<sup>14</sup> marked apolarity in solution (Medronho et al., 2012; Dufresne, 2017). Its  
<sup>15</sup> structural anisotropy, and its resulting amphiphilicity (Medronho et al., 2012),  
<sup>16</sup> are however reflected in the crystalline networks cellulose chains form in  
<sup>17</sup> living organisms such as plants, fungi, algae, bacteria, or tunicates (Moon  
<sup>18</sup> et al., 2011; Hamad, 2017). From the various allomorphs (Moon et al., 2011;  
<sup>19</sup> Dufresne, 2017), cellulose I(Nishiyama et al., 2003) and I (Nishiyama et al.,  
<sup>20</sup> 2002) are the only ones that may be found naturally in land plants (Moon  
<sup>21</sup> et al., 2011). They both reproduce on the nanocrystal level the anisotropy  
<sup>22</sup> of their monomeric unit. Indeed, cellulose chains assemble in sheets, parallel  
<sup>23</sup> to the equatorial planes of the anhydroglucose rings, which then stack up to  
<sup>24</sup> form multilayer crystalline structures, crystallites (Fig. 1.c) (Jarvis, 2003; Li  
<sup>25</sup> & Renneckar, 2011). Intra and intersheet cohensions are respectively insured  
<sup>26</sup> by interchain OH-O hydrogen bonds and by weaker interchain CH-O and  
<sup>27</sup> van der Waals interactions (Jarvis, 2003; Nishiyama, 2017). The formation  
<sup>28</sup> of these van der Waals interactions is thought to be the initial step through  
<sup>29</sup> which cellulose chains crystallize (Cousins & Brown, 1995).

<sup>30</sup> Hydrolysing cellulosic feedstocks in acidic conditions, usually with sul-  
<sup>31</sup> furic acid, digests their amorphous and non-cellulosic contents while mostly  
<sup>32</sup> preserving their crystalline parts (Dufresne, 2017; Moon et al., 2011; Hamad,  
<sup>33</sup> 2017). Under harsh enough conditions, the treatment yields highly crys-  
<sup>34</sup> talline cellulose-made particles, cellulose nanocrystals (CNCs). They are  
<sup>35</sup> hypothesized to be made of several adjacent crystallites (Uhlig et al., 2016;  
<sup>36</sup> Ding et al., 2012, 2014) assembled with a right-handed chirality (Usov et al.,  
<sup>37</sup> 2015). Introduction of sulfate half-ester groups at CNC surface during the

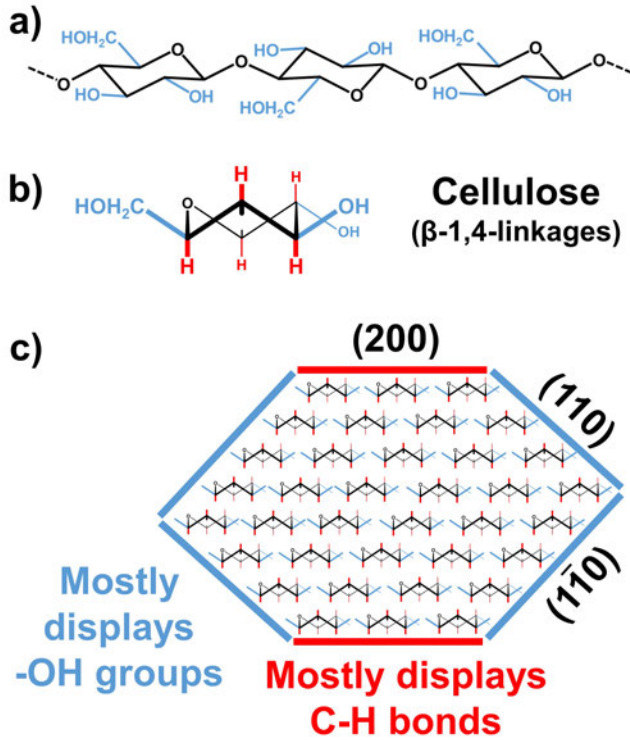


Figure 1: Anisotropy of cellulose. (a) Cellulose, a  $\beta$ -(1,4)-linked polymer of anhydroglucopyranose (French, 2017), has its monomeric units locked in a conformation where all their hydroxyl substituents (in blue) are in equatorial position while their C-H bonds (in red) are axial as exemplified in a profile view (b). (c) The structure of cellulose I crystallite reflects this anisotropy as cellulose chains are arranged in sheets held together by OH-O hydrogen bonds, which then stack-up through the formation of CH-O H-bonds and van der Waals interactions (Jarvis, 2003; Li & Renneckar, 2011). Based on Ding and Himmel's model (Ding & Himmel, 2006), the resulting crystallite displays up to three kind of surfaces corresponding to the lattice planes (110),  $(\bar{1}\bar{0})$ , and (200) of its crystalline unit. The latter displays mostly C-H bonds, while the two former are rich in hydroxyl groups.

38 hydrolysis provides them with an electrostatic stabilization upon suspension  
 39 in water and with interesting self-organization properties (Liu et al., 2011;  
 40 Hamad, 2017).

41 CNCs, especially sulfated ones, are usually described as polar particles,  
 42 which stems from the difficulty encountered to disperse them in non-polar  
 43 solvents and polymer matrices (Hamad, 2017). Although arising from exper-  
 44 imental observations, this description is at odd with the amphiphilic behav-  
 45 ior that can be expected from CNC anisotropic structure. Analysis of wide

46 (WAXS) and small angle X-ray scattering (SAXS) (Elazzouzi-Hafraoui et al.,  
 47 2008; Sèbe et al., 2012) as well as high resolution atomic force microscopy  
 48 (AFM) (Ding et al., 2006; 2012; 2014) indeed suggests that up to three kinds  
 49 of lateral surfaces are displayed by the nanocrystals extracted from cellulose  
 50 I sources (Fig. 1.c), by far the most common allomorph in higher plants  
 51 –wood included (Atalla & Vanderhart, 1999; Habibi et al., 2010). Within  
 52 the crystalline unit, they correspond respectively to the lattice planes (110),  
 53 ( $\bar{1}\bar{1}0$ ), and (200) (Ding & Himmel, 2006; Brown, 1996). The latter, parallel  
 54 to the sheets plane, displays mostly C-H bonds, while the two former in-  
 55 tersect the plane of the sheets and thus display hydroxyl groups (Fig. 1.c).  
 56 Molecular dynamic simulations suggests that (110) and ( $\bar{1}\bar{1}0$ ) surfaces have  
 57 similar hydrophilicity (Heiner et al., 1998; Matthews et al., 2006) and surface  
 58 energies (Yamane et al., 2006), while (200) surfaces are expected to be more  
 59 hydrophobic, with higher water contact angle (Mazeau & Rivet, 2008) and  
 60 lower surface energies (Yamane et al., 2006) (Table 1).

**Table 1: Cellulose nanocrystal surface properties according to the lattice plane displayed.**  
 $\tau$  is the total solubility parameter.  $\tau_D$ ,  $\tau_P$ , and  $\tau_H$  are its decomposition in term of  
 dispersive, polar, and hydrogen bonding components, respectively (Hansen, 2007).  $R_0$  is  
 the HSP radius.

Lattice plane		(110)	( $\bar{1}\bar{1}0$ )	(200)
Surface energy <sup>a</sup>	mN m <sup>-1</sup>	155	155	92
Water contact angle <sup>b</sup>		43	-	95
$\tau$	MPa <sup>1/2</sup>	31.3 1.4		19.2 2.7
$\tau_D$	MPa <sup>1/2</sup>	18.1 0.5		17.4 0.3
$\tau_P$	MPa <sup>1/2</sup>	20.4 0.5		4.8 0.5
$\tau_H$	MPa <sup>1/2</sup>	15.3 0.4		6.5 0.6
$R_0$	MPa <sup>1/2</sup>	7.8		2.1

<sup>a</sup> Modeled values as calculated by Yamane et al. (2006).

<sup>b</sup> Modeled values as calculated by Mazeau & Rivet (2008).

61 Chemically, a proof that CNCs display hydroxyl groups rich surfaces –  
 62 which would correspond to the (110) and ( $\bar{1}\bar{1}0$ ) lattice planes– may be pro-  
 63 vided easily by attempting to functionalize them (Eyley & Thielemans, 2014).  
 64 ( $\bar{1}\bar{1}0$ ) lattice planes have furthermore already been observed by atomic force  
 65 microscopy on cellulose I samples (Kuutti et al., 1995). The detection of un-  
 66 reactive C-H bonds rich surfaces –which would correspond to the (200) lattice  
 67 plane– is, however, harder to achieve. The main clue is that the display of  
 68 (200) lattice planes by CNCs should result in a certain level of amphiphilic-

69 ity, as experimentally confirmed : stable suspensions of CNCs in chloroform  
70 have been reported (Yu & Qin, 2012; Yu et al., 2012). This mildly non-polar  
71 solvent may also form inclusions in cellulose I fibers (Wade & Creely, 1974).  
72 It is worth noting that not every work reports a good dispersion in chloro-  
73 form (Yoo & Youngblood, 2016; Petersson et al., 2007) and it remains to  
74 be seen whether this divergence has to be attributed to differences in feed-  
75 stock, hydrolysis conditions, or protocol of dispersion, such as the intensity of  
76 the ultrasonication for instance. Other hydrophobic interactions of cellulose  
77 include those with cellulases (Himmel et al., 2007; Mazeau & Rivet, 2008)  
78 and congo red (Mazeau & Wyszomirski, 2012; Conley et al., 2017b,a) whose  
79 aromatic parts are both thought to adsorb primarily on the (200) surfaces.

80 Although these preliminary results point toward a chemical influence of  
81 (200) surfaces for some CNC suspensions, thus conforming WAXS, SAXS,  
82 and AFM observations, none of them really isolate their potential contribu-  
83 tion from the stronger influence of the (110) and (1̄10) surfaces.

84 In this work, we apply a thermodynamic approach based on the Hansen  
85 solubility parameters (HSP) and on sedimentation tests using 59 solvents and  
86 binary mixtures, to isolate experimentally the influence of the hydrophobic  
87 (200) surfaces from the predominant one of the more hydrophilic (110) and  
88 (1̄10) surfaces (as reported in Table 1). These investigations result into a  
89 mapping of CNC affinity for common solvents and polymers. The identifica-  
90 tion of an amphiphilic behavior for the nanocrystals establishes a direct link  
91 between their structure and their surface properties.

## 92 2. Materials and methods

### 93 2.1. Materials

94 CNCs, provided by Celluforce (Montreal, QC, Canada) as a spray-dried  
95 powder, were obtained from Kraft wood pulp by a sulfuric acid hydrolysis  
96 treatment followed by a neutralization with sodium hydroxide (NaOH). Pre-  
97 vious work from our team on CNCs from the same batch demonstrated that  
98 these particles are in average 165 nm long and 13 nm wide with a sulfur  
99 content equivalent of 3.4 sulfate half ester ( $O-SO_3H$ ) per 100 anhydroglucose  
100 units (Beuguel et al., 2018b). **The X-ray diffractogram is typical of I cellulose (Elazzouzi-Hafraoui et al., 2008; Sèbe et al., 2012)** and the crystallinity  
101 index was found to be of 81 %.

103 To obtain the dimensions of the CNCs the following procedure was ap-  
104 plied (Beuguel et al., 2018b). A drop of a sonicated water suspension of

105 CNCs, diluted at  $10 \mu\text{g}_{\text{CNCs}} \text{ mL}_{\text{water}}^{-1}$ , was deposited on a copper TEM grid  
106 covered by a 5 to 6 nm-thick layer of pure carbon. Average dimensions, with  
107 standard deviations in the range of 10 %, were obtained from measurements  
108 of over 100 particles performed on transmission electronic microscopy (TEM)  
109 micrographs obtained at 200 kV with a bright field imaging Jeol JEM 2100F  
110 (Beuguel et al., 2018b). The sulfur content was measured from X-Ray energy  
111 dispersive spectroscopy (EDX) analysis performed on the CNC spray-dried  
112 powder with a Tabletop Hitachi TM3030+ scanning electron microscope.  
113 Scanning of three samples on different locations, for a total of ten scans,  
114 yielded a sulfur over carbon (S/C) atomic ratio of 0.0057 with a standard  
115 deviation of 0.0005 (Beuguel et al., 2018b). The oxygen over carbon (O/C)  
116 atomic ratio was of 0.79 ± 0.02, very close to the theoretical value of 0.83  
117 for cellulose, and is indicative of a high level of purity for the nanocrystals  
118 (Siqueira et al., 2010). The CNC crystallinity was measured through X-ray  
119 diffraction (XRD) with a X'pert instrument (Philips) operating with Cu K  
120 radiations (wavelength of 0.1542 nm generated at 50 kV with a current of  
121 40 mA. Scan type was continuous with an angle  $\theta$  varying from 5.01 to  
122 49.99 with steps of 0.02 and a scan time of 1 s per step. The crystallinity  
123 index,  $I_C$ , was measured as  $I_C = 1 - I_{AM} / I_{200}$ , according to Segal's empirical  
124 method (Segal et al., 1959).  $I_{AM}$  and  $I_{200}$  are the intensities of the amorphous  
125 peak ( $2\theta = 18.85^\circ$ ) and of the peak corresponding to the (200) lattice planes  
126 ( $2\theta = 23.01^\circ$ ), respectively.

127 Organic solvents employed were purchased from commercial suppliers at  
128 high purity grade (purity >99 %, see Table A.1). The only exceptions are  
129 ethanol, used in its denatured form (purity of 95 %), and d-limonene (purity  
130 of 96 %), as higher purity grades of d-limonene are generally not available  
131 commercially. Distilled water was employed. Binary mixtures were prepared  
132 by mixing pure solvents. Densities and viscosities of solvents and mixtures  
133 at 25 °C were obtained by averaging experimental values reported in the  
134 specialized literature (Tables A.1&A.2).

135 *2.2. Sedimentation tests*

136 *2.2.1. Protocol*

137 10 mL of the different solvents and binary mixtures were added to 0.1 g  
138 of CNCs in a glass vials of radius 2.1 cm. An ultrasonic probe (Cole-Parmer)  
139 operating at a frequency of 20 kHz with a CV334 converter and a tapered  
140 microtip was used to disperse the CNCs. The treatment had a power of  
141 25 W and was applied with a pulse cycle ON OFF of 5 s 2 s for a total

142 energy of  $10,000 \text{ J g}_{\text{CNCs}}^{-1}$ . Previous experimentation demonstrated that such a  
 143 treatment do not result into desulfation of the CNCs (Beuguel et al., 2018b).  
 144 The vials were placed in an ice bath to avoid any overheating during the  
 145 ultrasonication. CNC suspensions ( $10 \text{ mg}_{\text{CNCs}} \text{ mL}_{\text{solv}}^{-1}$ ) were then allowed  
 146 to rest at  $25^\circ\text{C}$  for a relative sedimentation time,  $\text{RST} = 1.18 \cdot 10^{11} \text{ s}^2\text{m}^{-2}$ .  
 147 Calculated with Eq. 1 (Hansen, 2007), it corresponds for instance to an  
 148 absolute sedimentation time,  $t_{\text{sed}}$ , of 12.1 h in acetone, 48.0 h in water, or  
 149 1140 h in ethylene glycol (Tables A.1&A.2). Once the time of sedimentation  
 150 had elapsed, three kinds of qualitative behaviors were observed for CNC  
 151 sedimentation. Graded on a scale from best, 2, to worst, 0, they correspond  
 152 respectively to: 2- a suspension without formation of any sediment (as shown  
 153 in Fig. 2.a for DMSO), 1- a turbid suspension in which a sediment is formed  
 154 (dichloromethane), and 0- all remaining cases in which a sediment is formed  
 155 and the suspension is clear enough for text to be read through (toluene).  
 156 The only exception to the aforementioned protocol is the sedimentation in  
 157 triethanolamine, which was interrupted after a  $\text{RST}$  of  $1.18 \cdot 10^{10} \text{ s}^2\text{m}^{-2}$  (10%  
 158 of the standard  $\text{RST}$ ). Due to the very high viscosity of triethanolamine, it  
 159 corresponds to a time of sedimentation  $t_{\text{sed}}$  of 4100 h. Its behavior is clearly  
 160 that of a 0-grade solvent (Fig. A.1).

$$t_{\text{sed}} = \text{RST} \frac{\text{solv}}{\text{CNCs}} \quad (1)$$

### 161 2.2.2. RST calibration

162 Sulfating CNCs provides them with surface charges, generating electro-  
 163 static stabilization. It is a kinetic effect: the thermodynamically favored  
 164 outcome of a colloidal suspension is the coagulation of the particles (Kron-  
 165 berg et al., 2014). For electrostatic stabilization to manifest, there has to  
 166 be dissociation between the negatively charged CNCs and their counter-ions,  
 167 an outcome favored in solvents whose dielectric constants,  $\epsilon_{\text{solv}}$ , are high  
 168 (Kronberg et al., 2014). HSP characterization is a thermodynamic approach  
 169 and a  $\text{RST}$  of  $1.18 \cdot 10^{11} \text{ s}^2\text{m}^{-2}$  was selected following a calibration aimed at  
 170 minimizing the influence of such kinetic effects on the sedimentation results.

171 At low  $\text{RST}$ , sedimentation results were strongly correlated with the di-  
 172 electric constants of the solvents (Table A.1). Quickly, a discrimination how-  
 173 ever appears among highly dielectric solvents and, at a  $\text{RST}$  of  $5.9 \cdot 10^{10} \text{ s}^2\text{m}^{-2}$ ,  
 174 we were already able to hint “good” solvents from “poor” ones independently  
 175 of their dielectric constant. At  $\text{RST} = 1.18 \cdot 10^{11} \text{ s}^2\text{m}^{-2}$ , results are no

longer correlated with the dielectric constants. Highly dielectric solvents like methanol ( $\epsilon_{\text{solv}}=33.0$ ), ethylene glycol (41.4), DMF (38.3), or propylene carbonate (66.1) received the grade 0, while DMSO (47.2) or ethanolamine (31.9) are at 2. The state of sedimentation at  $\text{RST} = 1.18 \cdot 10^{11} \text{ s}^2\text{m}^{-2}$  was found to be meta-stable as increasing the  $\text{RST}$  beyond  $1.18 \cdot 10^{11} \text{ s}^2\text{m}^{-2}$  no longer affects the results. Vials were kept for months and in volatile media such as chloroform and dichloromethane, the solvent was fully evaporated before any significant change in the suspension turbidity could be observed. It does not mean that the electrostatic stabilizing effect is no longer felt at  $\text{RST} = 1.18 \cdot 10^{11} \text{ s}^2\text{m}^{-2}$ , but that electrostatic stabilization alone is no longer sufficient to prevent sedimentation at this point. For particles to remain in suspension at high  $\text{RST}$ , and whatever the level of electrostatic stabilization, there has to be a certain level of chemical affinity. It is this chemical affinity that the HSP analysis seeks to capture.

### 2.3. Thermodynamic approach - Hansen solubility parameters

#### 2.3.1. Background

Initially developed to address the issue of the dispersibility of the various components of paints, solubility -or cohesion- parameters theory aims at quantifying the cohesive energy density (taken equal to  $\frac{1}{2} \epsilon$ , MPa) between a chemical and its neighboring media (Hildebrand & Scott, 1950, 1962; Hansen, 2007). Hansen proposed to split the total cohesion parameter  $\chi$ , into its three main components resulting from the London dispersion forces  $\chi_D$ , the dipole-dipole interactions  $(\chi_P)$ , and hydrogen bonding interactions  $(\chi_H)$  (Hansen 1967a,b, 2007; Hansen & Skaarup, 1967). The linearity of the decomposition in terms of energies means that square may then be written as the sum of the squared HSP (Eq. 2). In the HSP theory, every chemical may be represented by a triplet  $(\chi_D, \chi_P, \chi_H)$ , and then be plotted in a 3 dimensional graph (Hansen, 2007). HSP values of solvents may be determined directly experimentally or estimated by group contribution methods and are now tabulated, alongside those of many commodity polymers (Hansen, 1967b, 2007; Abbott et al., 2018). Gardebjer et al. (2016) used one of these group contribution methods to estimate the HSP of cellulose's repeating unit, cellobiose. They computed a value of  $(\chi_D, \chi_P, \chi_H) = (16.3; 16.2; 20.7) \text{ MPa}^{1/2}$  and assumed it to be the HSP values of CNCs (Gardebjer et al., 2016). Although it provided a quick and easy estimate, the method is unsatisfactory as it does not take into account the fact that polymer HSP are almost systematically greater than those of their repeating units, nor the

213 fact that crystallinity may greatly affect HSP values (Hansen, 2007; Abbott  
 214 et al., 2018). Unknown HSP may be determined more accurately through an  
 215 indirect approach. Affinity tests between the material and various solvents  
 216 are conducted with the idea that, “like seeking like”, the stronger are the  
 217 interactions the shorter is the distance,  $R_a$  (MPa $^{1/2}$ , Eq. 3), between their  
 218 respective Hansen solubility parameters (Hansen, 2007). “Good” solvents,  
 219 where the “goodness” may be assigned quantitatively (e.g. maximum solu-  
 220 bility) or qualitatively (e.g. suspension turbidity or swelling behavior), thus  
 221 describe a sphere of radius  $R_0$  (MPa $^{1/2}$ ), whose center corresponds to the  
 222 unknown’s HSP (Hansen, 2007). The set of solvents may be completed by  
 223 mixtures (Machui et al., 2012), Their HSP ( $D_{mix}$ ;  $P_{mix}$ ;  $H_{mix}$ ) were calcu-  
 224 lated through Eq. 4 (Hansen, 2007), in which ( $D_i$ ;  $P_i$ ;  $H_i$ ) are the HSP  
 225 values of the constituent  $i$  and  $v_i$  its volume fraction;  $n$  is the total number  
 226 of solvents in the mixture.

$$\frac{2}{T} = \frac{2}{D} + \frac{2}{P} + \frac{2}{H} \quad (2)$$

$$R_a^2 = 4 \left( \frac{(D_{1,n})^2 + (D_{2,n})^2}{n} + \frac{(P_{1,n})^2 + (P_{2,n})^2}{n} + \frac{(H_{1,n})^2 + (H_{2,n})^2}{n} \right) \quad (3)$$

$$D_{mix} = \sum_{i=1}^n v_i D_i ; P_{mix} = \sum_{i=1}^n v_i P_i ; H_{mix} = \sum_{i=1}^n v_i H_i \quad (4)$$

227 Our set of solvents was selected based on their position in the HSP graph  
 228 to maximize the coverage and based on the uncertainty of the solvents’ HSP  
 229 coordinates. Indeed, the indirect method of HSP determination for an un-  
 230 known compound is no more precise than that of the solvents that are em-  
 231 ployed to perform the characterization. Historically, HSP coordinates were  
 232 determined experimentally for a set of 90 common solvents, from which group  
 233 contribution models have been derived (Hansen, 2007). Nowadays, and based  
 234 on these group contribution methods, HSP of thousands of solvents have  
 235 been calculated (Hansen, 2007; Abbott et al., 2018). When we selected our  
 236 27 pure solvents, we aimed at picking them from the list of the 90 experimen-  
 237 tally confirmed solvents. Exceptions to the list are ethyl benzoate, heptane,  
 238 d-limonene, triethanolamine, and water. Water, with its three sets of HSP,  
 239 is a special case (see Hansen 2007). Heptane, being purely dispersive, has a  
 240 low uncertainty (uncertainty arises mostly from the calculation of the polar  
 241 and hydrogen-bonding components:  $P$  and  $H$ , respectively) (Abbott et al.,  
 242 2018). Ethyl benzoate, d-limonene, and triethanolamine HSP values have

been calculated, rather than empirically determined, inducing a greater uncertainty. They were nonetheless selected for their interesting position in the HSP graph.

### 2.3.2. HSP analysis

HSP analysis was performed with the software HSPiP (Abbott et al., 2018). HSP values of pure solvents, binary mixtures, and polymers, were extracted from the HSPiP database (Abbott et al., 2018) and are respectively provided in Tables A.1, A.2, and A.3.

For the sphere fitting, we considered both grade 1 and grade 2-solvents (and mixtures) to be “good” and grade 0-ones to be “poor”. The algorithm of the software maximizes the function **FIT** described below (Eq. 6) (Hansen, 2007; Abbott et al., 2018). The ideal result is a sphere of center ( $D_s$ ;  $P_s$ ;  $H_s$ ) and of radius  $R_0$  that contains all the “good” solvents and mixtures while excluding any “poor” ones. A solvent/mixture is located in the sphere if its distance to the sphere’s center,  $R_a$  (Eq. 2), is smaller than or equal to  $R_0$ . It corresponds to a reduced energy difference **RED**  $\leq 1$  (Eq. 5).

$$RED = R_a/R_0 \quad (5)$$

The quality of the fitting may be assessed through the **FIT** value and through the uncertainty on the ( $D_s$ ;  $P_s$ ;  $H_s$ ) coordinates (Hansen, 2007; Abbott et al., 2018). **FIT** (Eq. 6) is a desirability function (Hansen, 2007) that provides information about the quality of the fit on the  $m$  solvents tested : indeed, a “poor” solvent/mixture located inside a sphere (**RED**  $\leq 1$ ) or a “good” one located outside (**RED**  $> 1$ ) induces a penalty on the **FIT** coefficient. The better the fit, the closest **FIT** will be from 1.0 (**FIT**  $\geq 1.0$ ). The uncertainty “( $D_s$ ;  $P_s$ ;  $H_s$ )” provides information on the tightness of the HSP sphere core’s position. Values in the range of  $0.25\text{--}0.50 \text{ MPa}^{1/2}$  are indicative of a very good fit and of a tight core, while a poor fit will result in uncertainties in the range of  $1 \text{ MPa}^{1/2}$  (Abbott et al., 2018). It is possible to have a tight core for two parameters and a loose one for the last, meaning that there is a lack of data points in that direction (Abbott et al., 2018). It has to be noted that fitting a sphere on less than 4-5 good solvents necessarily leads to an uncertainty that may not be reflected in the **FIT** value nor in the “( $D_s$ ;  $P_s$ ;  $H_s$ )”. The existence of an uncertainty means that results obtained in running several times the algorithm on the same data differ slightly. Results reported here are those corresponding to

277 the highest FIT value and the lowest uncertainty over at least 10 runs of the  
 278 fitting algorithm. The values were overall very stable between the different  
 279 fits with variations in the range of 0.001 for FIT and of 0.05 MPa<sup>1/2</sup> for  
 280 the different uncertainties: (D<sub>s</sub>; P<sub>s</sub>; H<sub>s</sub>) .

$$FIT = \frac{m}{\sum_{i=1}^{1/m} A_i}$$

(6)

For "good" solvents inside a sphere : A<sub>i</sub> = 1

For "poor" solvents outside a sphere : A<sub>i</sub> = 1

For "good" solvents outside a sphere : A<sub>i</sub> = e<sup>+(R<sub>0</sub>-R<sub>a</sub>)</sup>

For "poor" solvents inside a sphere : A<sub>i</sub> = e<sup>+(R<sub>a</sub>-R<sub>0</sub>)</sup>

### 281 3. Results and discussion

282 Considering both grade 2 and 1 as good solvents, two distinct regions of  
 283 preferential dispersibility may clearly be distinguished. The first is in the po-  
 284 lar region of the graph (high P and H, Fig. 2.c) and contains all of the grade  
 285 2 solvents: dimethylsulfoxide (DMSO), formamide, water, and ethanolamine.  
 286 The area delimited by these solvents is bordered by 0-grade ones like tri-  
 287 ethanolamine, propylene carbonate, N,N-dimethylformamide, or acetone. A  
 288 second distinct region may then be distinguished in the mildly non-polar  
 289 region (intermediate P and H) where chloroform and dichloromethane are  
 290 classified as grade 1 and stand alone surrounded by poor solvents. This  
 291 behavior, with two distinct regions, is expected in the HSP theory for am-  
 292 phiphilic species such as particles or block copolymers for instances (Hansen,  
 293 2007). In this con guration, two HSP spheres, which correspond to the dif-  
 294 ferent a nities of the chemical, may be drawn.

295 For a better HSP fit, sedimentation tests were performed for binary mix-  
 296 tures of DMSO + acetone, toluene, and methanol, and binary mixtures of  
 297 formamide + methanol and 1-propanol. Results obtained with binary mix-  
 298 tures validate our scale of dispersibility as the goodness of a grade 2 solvent  
 299 like DMSO decreases to grade 1 once 40 vol% of methanol, a grade 0 solvent,  
 300 is added and then to 0 beyond 60 vol% (Fig. A.2.b&e). DMSO is known  
 301 to be one of the best solvent for CNCs dispersion as it enables strong gel  
 302 formation upon heating (Sojoudiasli et al., 2017).

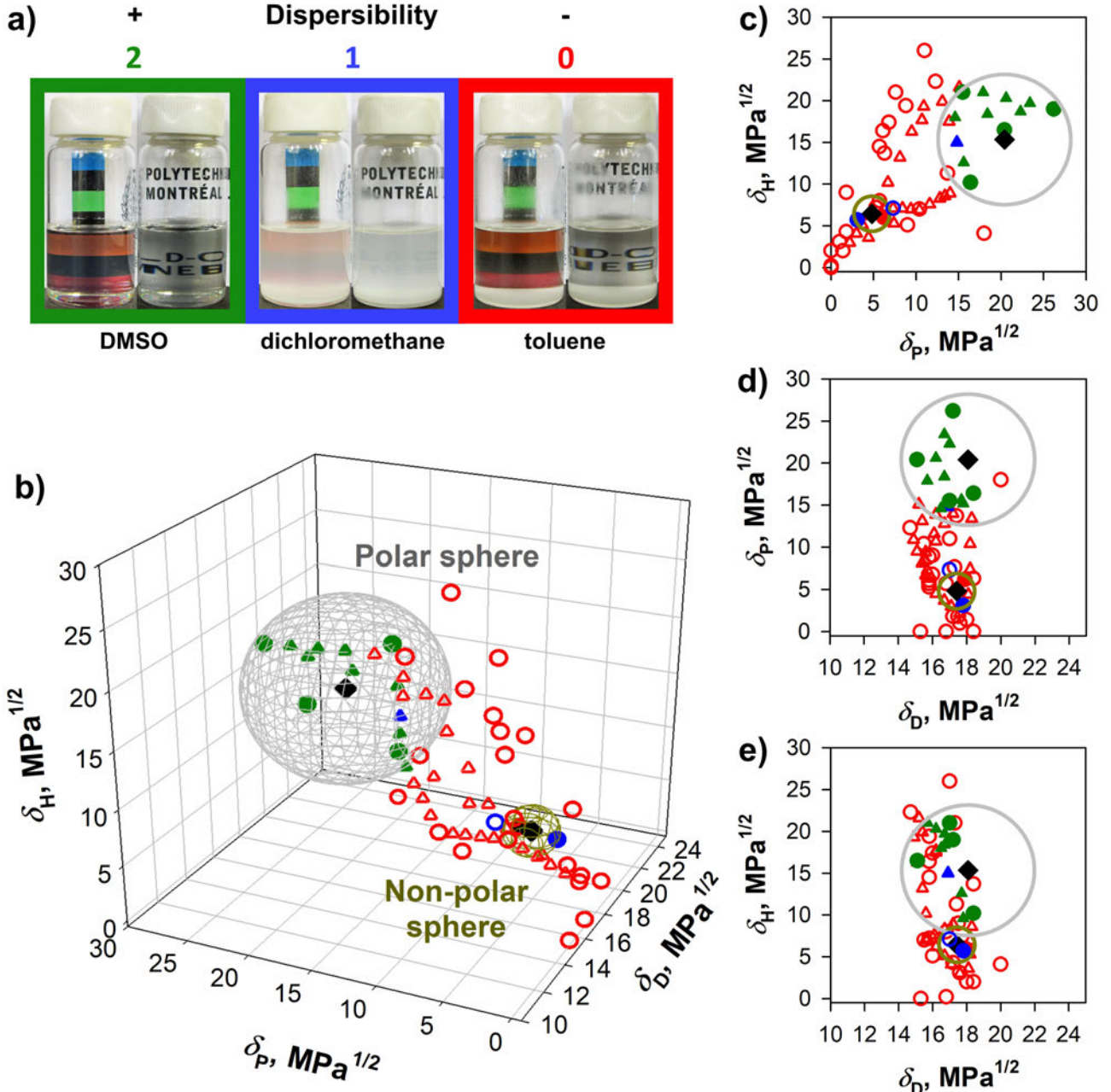


Figure 2: HSP graph of wood-based sulfuric acid-hydrolyzed CNCs.(a) CNC scale of dispersibility. Three different grades were attributed to the CNC state of dispersion, from best to worst: 2-in green-No sediment at the bottom of the vial, 1-in blue-Presence of a sediment, the suspension is too turbid to be able to read a text through, 0-in red-Presence of a sediment, the suspension is less turbid/clear. Pure solvents are represented by circles, binary mixtures by triangles, sphere centers by black diamonds. Two different spheres may be plotted : a large polar sphere ( $\delta_D$ ;  $\delta_P$ ;  $\delta_H$ ) = (18.1; 20.4; 15.3) (0.5; 0.5; 0.4) MPa $^{1/2}$  and another smaller sphere in the mildly non-polar region ( $\delta_D$ ;  $\delta_P$ ;  $\delta_H$ ) = (17.4; 4.8; 6.5) (0.3; 0.5; 0.6) MPa $^{1/2}$ . Symbols located inside a sphere are full and symbols outside are empty. The HSP graph is represented in a 3-dimensional view(b), and in 2-dimensional views alongside the planes H- P (c), P- D (d), and H- D (e).

Using HSPiP (Hansen Solubility Parameters in Practice) software (Abbott et al., 2018), it was possible to obtain a well defined sphere ( $FIT = 1.0$ , see Eq. 6) of radius  $R_{0,P}=7.8 \text{ MPa}^{1/2}$  in the polar region. It includes 13 good solvents and mixtures while excluding any poor ones. Its center's coordinates ( $D; P; H$ ) are  $(18.1; 20.4; 15.3) - (0.5; 0.5; 0.4) \text{ MPa}^{1/2}$  for a  $\tau$  of  $31.3 - 1.6 \text{ MPa}^{1/2}$ . Having defined with precision what stands clearly for the dominant affinity of CNCs, the case of chloroform and dichloromethane may be addressed. These results are concordant with reports by Yu et al. of stable suspensions of sulfuric acid hydrolyzed CNCs in chloroform (Yu & Qin, 2012; Yu et al., 2012). A fitting in this area of the graph yields a  $FIT$  of 0.974 with a sphere of radius  $R_{0,P}=2.1 \text{ MPa}^{1/2}$  and centered about  $(D; P; H) = (17.4; 4.8; 6.5) - (0.3; 0.5; 0.6) \text{ MPa}^{1/2}$ . It corresponds to a  $\tau$  of  $19.2 - 2.7 \text{ MPa}^{1/2}$ . Here, the  $FIT$  value is lowered by ethyl benzoate, which is a 0-grade solvent despite having HSP close to that of dichloromethane and chloroform. It is not clear whether it highlights a limitation of the HSP method itself –as we know that conformation effects for instance are not accounted for in HSP theory– or a limitation of the HSP group contribution models. Ethyl benzoate is indeed among the few solvents we employed whose HSP were calculated without any experimental confirmation (Hansen, 2007). It may thus be that the  $FIT$  value is only lowered by imprecise solvent coordinates: ethyl benzoate while being plotted as inside of the non-polar sphere (Fig. 2) may actually be out of it. From the 90 solvents experimentally proofed by Hansen and co-workers (1967; 1967a; 1967b), and aside from chloroform and dichloromethane, none is located in the area of interest. This issue cannot be settled easily with the current experimental method. Fitted using only two good solvents, the position of the non-polar sphere thus has to be considered with caution. It however provides the first experimental estimates of CNC hydrophobic surface HSP.

The polar sphere is considered to correspond to the HSP of the hydroxyl rich  $(110)$  and  $(\bar{1}\bar{1}0)$  surfaces. Computer simulations indeed predicts that  $(110)$  and  $(\bar{1}\bar{1}0)$  surfaces have similar surface energies (Yamane et al., 2006) and hydrophilicity (Heiner et al., 1998; Matthews et al., 2006), which means that they are expected to be represented by a single HSP sphere (Table 1). Meanwhile, the mildly non-polar sphere is attributed to the display of  $(200)$  surfaces by the nanocrystals. Their lower simulated surface energy (Yamane et al., 2006) and higher modeled water contact angle (Mazeau & Rivet, 2008) are indeed expected to result into a distinct HSP sphere.

The contrast between the better fit and wider radius of the polar sphere

and the lesser ones of the non-polar sphere is coherent with the fact that sulfuric acid hydrolyzed CNCs have been reported to exhibit experimentally a predominant polar and hydrophilic behavior. HSP of the polar sphere are furthermore very close to those obtained for the chemical accessibility of cellulose : ( $\text{D}$ ;  $\text{P}$ ;  $\text{H}$ ) = (19.09; 15.77; 15.29) (0.15; 0.25; 0.30) MPa $^{1/2}$  (Hansen & Björkman, 1998; Larsson & Johns, 1988; Minhas & Robertson, 1967). These are calculated from the ability of different solvents to swell cotton-based I cellulose pulp. Swelling increases the active surface area of the pulp by increasing hydroxyl group accessibility, the amount of which is quantified chemically through a thallation of the -OH functions (Minhas & Robertson, 1967). The only significant deviation lies in  $\text{P}$ , the polar component, that is increased by +4.6 MPa $^{1/2}$  from the chemical accessibility of cellulose HSP to our polar sphere's results. Slight variations in  $\text{D}$  and  $\text{H}$ , coupled to a sharp increase in  $\text{P}$  are coherent with the effect of surface sulfatation based on the predictions of HSP group contributions (Stefanis & Panayiotou, 2008). The  $\text{P}$  increase for CNCs with respect to the cotton-based pulp is thus attributed to the introduction of sulfate groups on the hydroxyl groups of the nanocrystal surfaces during the sulfuric acid hydrolysis (Hamad & Hu, 2010; Hamad, 2017). Part of this variation is also probably imputable to the difference in wettability between I and I hydroxyl-rich surfaces, although simulations predict very similar surface energies with 154 mN m $^{-1}$  and 155 mN m $^{-1}$ , respectively (Yamane et al., 2006).

It is worth noting that this shift of +4.6 MPa $^{1/2}$  in  $\text{P}$  reduces the HSP distance of CNCs with water from 9.3 MPa $^{1/2}$  to 6.1 MPa $^{1/2}$ , which may be able to partly explain the increased affinity of sulfated CNCs for water. As contact angles have usually been found experimentally to be positively correlated with HSP distance (Hansen, 2007), this finding is also coherent with the water contact angle value obtained by simulation by Mazeau & Rivet (2008). The 43° of the (110) surface corresponds to a HSP distance of 6.1 MPa $^{1/2}$ , while the 95° of the (200) surface corresponds, based on our results, to a HSP distance of 19.1 MPa $^{1/2}$ .

From our knowledge of the CNC structure, it is thus possible to assign each of the spheres to a lattice plane, which enables us for the first time to estimate the amphiphilicity of wood-based sulfated CNCs. Our results also highlight the limitations of group contribution methods to estimate cellulose nanocrystal HSP. Given that they do not take into account conformation effects, computations by Gardebjer et al. (2016) were not able to predict a second non-polar sphere for CNCs. If we compare their results to those

of our polar sphere, they also underestimate  $\sigma$  and  $\rho$  by  $1.7 \text{ MPa}^{1/2}$  and  $4.2 \text{ MPa}^{1/2}$ , respectively, which is not unexpected when HSP of a polymer are compared to those of its repeating unit (Hansen, 2007). The hydrogen bonding component,  $\mu$ , was underestimated by  $5.4 \text{ MPa}^{1/2}$  (Gardebjer et al., 2016). It may probably be attributed to the fact that the influence of the -OH groups of cellulose is hindered by their involvement in the crystalline network of CNCs (Jarvis, 2003; Djahedi et al., 2016).

The amphiphilicity of cellulose chains has recently been advanced as a key-factor to explain the low solubility of cellulose chains in polar solvents (Medronho et al., 2012). This parameter was not considered by Hansen & Björkman (1998) when they worked on wood ultrastructure and cellulose affinity. While Fig. 2 provides experimental evidence for this amphiphilicity, we believe that due to the high dependency of HSP with conformation effects, such as those induced by crystallinity (Hansen, 2007; Abbott et al., 2018), any extrapolation from crystalline to amorphous cellulose has to be considered with great caution. Our interest in HSP instead lies in their ability to represent in a same graph –thus enabling comparisons– chemicals of very different scales, from solvents to polymers, (nano)particles, and macro-scale surfaces. Determining HSP of cellulose nanocrystals, based on their behavior in a set of solvents, may thus provide information about their affinity for polymer matrices. HSP of some common polymer matrices, such as poly(vinyl alcohol) (PVOH), poly(lactic acid) (PLA), poly(ethylene glycol) (PEG), poly(methyl methacrylate) (PMMA), poly(ethylene) (PE), and poly(propylene) (PP), are available (Abbott et al., 2018) and are plotted in the Fig. 3. It is worth pointing out that the HSP values of polymers are notably functions of their molecular weight and degree of crystallinity (Hansen, 2007; Abbott et al., 2018) and the parameters employed here are average values as provided in the HSPiP polymer dataset (Abbott et al., 2018). These polymers may be split into 3 groups based on their HSP: I-in the polar sphere (PVOH), II-in between the spheres (PEG, PLA, PMMA) and III-in the non-polar region (PE and PP). CNC-polymer affinity is not the only factor at play for CNC dispersion in polymer matrices.

The protocol employed (melt mixing or solvent casting) has, for instance, a major influence (Bagheriasl et al., 2016, 2017). Assuming that the quality of CNC dispersion in the solvent is important for solvent casting, then other parameters such as the "goodness" of the solvent (Fig. 2), the initial state of CNCs (Beuguel et al., 2018b; Peng et al., 2016) –the use of never-dried, freeze-dried, or spray-dried–, and the protocol employed for the dispersion –such as

417 ultrasonication conditions (Beuguel et al., 2018a)– are also relevant. Keeping  
418 these points in mind, it is striking how these polymer-categories (I, II, and  
419 III), based solely on HSP, match with the experimental quality reported  
420 for the dispersion of sulfuric acid-hydrolyzed CNCs in the aforementioned  
421 matrices: PVOH has been reported to be one of the best matrices for CNC  
422 dispersion both in solvent casting and melt mixing (Hamad, 2017), which  
423 is coherent with it being in the dominant polar sphere of CNCs. A good  
424 dispersion of CNCs is also achievable in PLA (Zhang et al., 2015; Bagheriasl  
425 et al., 2016, 2017), PEG (Beuguel et al., 2018a; Yao et al., 2017; Zhou et al.,  
426 2011; Xu et al., 2013, 2014), and PMMA (Yin et al., 2016) through a solvent  
427 casting. Direct melt mixing may however remain difficult for this group II-  
428 polymers as in the case of PLA (Raquez et al., 2013; Khoshkava & Kamal,  
429 2013; Dhar et al., 2016; Bagheriasl et al., 2017).

430 Dhar et al. (2016) demonstrated that the sulfatation of CNC surfaces  
431 lessens their dispersibility in PLA matrices, which is consistent with our  
432 HSP results: the shift of  $+4.6 \text{ MPa}^{1/2}$  in the  $\rho$  of the polar sphere between  
433 sulfated CNCs and chemically accessible cellulose increases the distance be-  
434 tween the PLA matrices and the (110) and (1 $\bar{1}$ 0) surfaces' sphere from 11.4  
435 to 15.0  $\text{MPa}^{1/2}$ . Based on the HSP theory, the absence of any adsorption  
436 of PEG on CNC surfaces (Beuguel et al., 2018a; Reid et al., 2017) is also  
437 coherent with this polymer being out of any sphere, adsorption being only  
438 expected for compounds of very similar HSP (Hansen, 1997). Modification  
439 of the nanocrystal OH groups, which is expected to result in a shift of the  
440 corresponding surfaces HSP sphere (Peng et al., 2016; Yoo & Youngblood,  
441 2016), may significantly improve the CNC dispersion and the reinforcing ef-  
442 fect in group II-matrices (Raquez et al., 2013; Yin et al., 2016; Zhang et al.,  
443 2015; Khoshkava & Kamal, 2013). It is likely that a systematic HSP char-  
444 acterization of the modified CNCs would have concluded that any chemical  
445 modification that improves the CNC dispersion in a matrice also reduces  
446 the HSP distance between the polar sphere and this matrix, as in the case  
447 of Peng et al. (2017). In group III-matrices such as PP (Bagheriasl et al.,  
448 2015; Khoshkava & Kamal, 2014) and PE (Lewandowska & Eichhorn, 2016;  
449 Inai et al., 2018), nanoscale dispersion in melt compounding seems to be  
450 impossible without the use of a compatibilizer. While unmodified nanocrys-  
451 tals have an interfacial tension with PP more than fourfold that with PLA,  
452 surface modification may, here again, shift the relative affinity of CNCs and  
453 make dispersion more favorable in PP with a slightly lower interfacial ten-  
454 sion (Khoshkava & Kamal, 2014). Probably due to the low solubility of

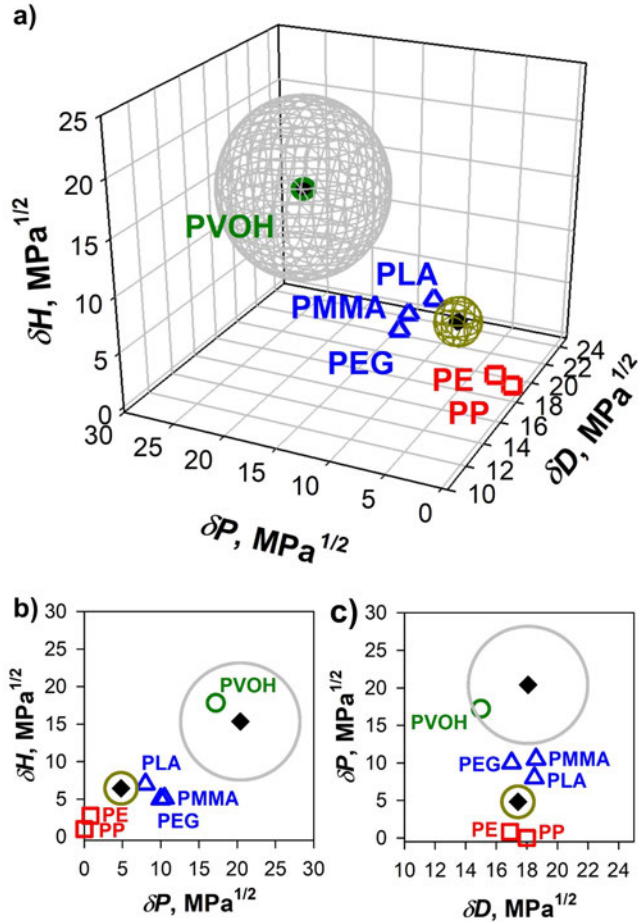


Figure 3: HSP graph of wood-based sulfuric acid hydrolyzed CNCs (see Fig. 2) compared to some commodity polymers. These polymers may be split into 3 groups based on their HSP (Abbott et al., 2018): I-green circles-in the polar sphere for poly(vinyl alcohol) (PVOH); II-blue triangles-in between the spheres for poly(lactic acid) (PLA), poly(ethylene glycol) (PEG), and poly(methyl methacrylate) (PMMA); and III-red squares-in the non-polar region for poly(ethylene) (PE), and poly(propylene) (PP). Categories I, II, and III match, from best to worst, with experimental reports for the dispersibility of CNCs in these matrices. The HSP graph is represented in a 3-dimensional view (a), and in 2-dimensional views alongside the planes  $H - P$  (b), and  $P - D$  (c).

455 these polymers in common solvents (Hansen, 2007), no experimental data  
 456 are available for the solvent casting of these PP and PE nanocomposites.

457 4. Concluding remarks

458 In conclusion, we linked CNC dispersibility in a large set of solvents and  
459 binary mixtures to the anisotropy of the nanocrystal structure. Wood-based  
460 sulfuric acid-hydrolyzed CNCs were found to be predominantly polar par-  
461 ticles with a main HSP sphere of radius  $7.8 \text{ MPa}^{1/2}$  and of center ( $D ; P$   
462 ;  $H$ ) = (18.1; 20.4; 15.3) (0.5; 0.5; 0.4)  $\text{MPa}^{1/2}$ . This main behavior is  
463 thought to reflect the influence of their hydroxyl-rich (110) and (1 $\bar{1}$ 0) surfaces  
464 and is coherent with their behavior described in the literature. While pre-  
465 dicted years ago through simulations and expected based on cross-sectional  
466 structure analysis of the nanocrystals through X-ray scattering and AFM  
467 techniques, this study is the first to experimentally confirm the contribution  
468 of **hydrophobic surfaces** to the behavior of CNCs in suspensions. We pro-  
469 vide an approximation of their chemical influence through the determination  
470 of their Hansen solubility parameters (HSP). Although refinements are still  
471 necessary, as based only on two good solvents, the non-polar sphere location  
472 is estimated in the range of (17.4; 4.8; 6.5) (0.3; 0.5; 0.6)  $\text{MPa}^{1/2}$  with a  
473 radius of  $2.1 \text{ MPa}^{1/2}$ . This position, relatively to that of the polar sphere, is  
474 coherent with results from computer simulations **for the display of (200) lat-**  
475 **tice planes by the CNC particles.** Further work is required to determine the  
476 influence of the feedstock, of the hydrolysis conditions, and of the dispersion  
477 protocol on the display of an amphiphilic behavior by CNCs.

478 HSP graphs are a useful tool to predict the CNC dispersion in polymer  
479 matrices and allow us a better understanding of results already published in  
480 the literature. Such characterization could be carried out on functionalized  
481 particles to understand the effect of the chemical modification on the surface  
482 properties of the nanocrystals (Yoo & Youngblood, 2016; Peng et al., 2016)  
483 and on their dispersibility (Peng et al., 2017) in non-polar media.

484 Conflicts of interest

485 There are no conflicts to declare

486 Acknowledgments

487 The authors acknowledge the financial contributions of FPIInnovations  
488 (Pointe-Claire, QC, Canada), of PRIMA Québec (grant number FPI NCC  
489 RD001), of the National Science and Engineering Research Council (NSERC,

490 grant number RDCPJ 490786-15). The Fond de Recherche du Québec - Na-  
491 ture et Technologies (FRQNT) kindly provided C. Bruel with a scholarship  
492 (number 208324). Celluforce (Montréal, QC, Canada) is also gratefully ac-  
493 knowledged for providing the cellulose nanocrystals. The authors would like  
494 to thank Dr. W. Y. Hamad, from FPIInnovations, for his contribution in  
495 reviewing this work. We are grateful to Dr. Q. Beuguel for his contribution  
496 to the TEM and EDX analyses. Finally, Mr. J.-P. Masse is acknowledged  
497 for his help with the XRD analysis.

498 **References**

- 499 Abbott, S. J., Hansen, C. M., & Yamamoto, H. (2018). Hansen solubility  
500 parameters in practice software, ebook, datasets. Url: <http://www.hansen->  
501 solubility.com, accessed on 2018/07/03.
- 502 Atalla, R. H., & Vanderhart, D. L. (1999). The role of solid state  $^{13}\text{C}$  NMR  
503 spectroscopy in studies of the nature of native celluloses. *Solid State Nucl.*  
504 *Magn. Reson.*, 15, 1–19.
- 505 Bagheriasl, D., Carreau, P. J., Dubois, C., & Riedl, B. (2015). Proper-  
506 ties of polypropylene and polypropylene/poly(ethylene-co-vinyl alcohol)  
507 blend/CNC nanocomposites. *Compos. Sci. Technol.*, 117, 357–363.
- 508 Bagheriasl, D., Carreau, P. J., Riedl, B., Dubois, C., & Hamad, W. Y.  
509 (2016). Shear rheology of polylactide (PLA)-cellulose nanocrystal  
510 (CNC) nanocomposites. *Cellulose*, 23, 1885–1897.
- 511 Bagheriasl, D., Safdari, F., Carreau, P. J., Dubois, C., & Riedl, B. (2017).  
512 Development of cellulose nanocrystal-reinforced polylactide: A compara-  
513 tive study on different preparation methods. *Polym. Compos.*, . DOI:  
514 10.1002/polc.24676.
- 515 Beuguel, Q., Tavares, J. R., Carreau, P. J., & Heuzey, M.-C. (2018a). Rheo-  
516 logical behavior of cellulose nanocrystal suspensions in polyethylene glycol.  
517 *J. Rheol.*, 62, 607–618.
- 518 Beuguel, Q., Tavares, J. R., Carreau, P. J., & Heuzey, M.-C. (2018b). Ul-  
519 trasonication of spray- and freeze-dried cellulose nanocrystals in water. *J.*  
520 *Colloid Interface Sci.*, 516, 23–33.

- 521 Brown, R. M. (1996). The biosynthesis of cellulose. *J. Macromol. Sci., Part*  
522 **A: Pure Appl. Chem.**, A33, 1345–1373.
- 523 Chaturvedi, K., Ganguly, K., Kulkarni, A. R., Kulkarni, V. H., Nadagouda,  
524 M. N., Rudzinski, W. E., & Aminabhavi, T. M. (2011). Cyclodextrin-based  
525 siRNA delivery nanocarriers: a state-of-the-art review. **Expert Opin. Drug**  
526 **Del.**, 8, 1455–1468.
- 527 Conley, K. M., Godbout, L., Whitehead, M. A., & van de Ven, T. G. M.  
528 (2017a). Reversing the structural chirality of cellulosic nanomaterials. **Cell-**  
529 **ulose**, 24, 5455–5462.
- 530 Conley, K. M., Whitehead, M. A., & van de Ven, T. G. M. (2017b). Probing  
531 the structural chirality of crystalline cellulose with induced circular  
532 dichroism. **Cellulose** 24, 479–486.
- 533 Cousins, S. K., & Brown, R. M. (1995). Cellulose I microfibril assembly:  
534 computational molecular mechanics energy analysis favours bonding by  
535 van der Waals forces as the initial step in crystallization. **Polymer**, 36,  
536 3885–3888.
- 537 Dhar, P., Bhasney, S. M., Kumar, A., & Katiyar, V. (2016). Acid function-  
538 alized cellulose nanocrystals and its effect on mechanical, thermal, crys-  
539 tallization and surfaces properties of poly (lactic acid) bionanocomposites  
540 films: A comprehensive study. **Polymer**, 101, 75–92.
- 541 Ding, S.-Y., & Himmel, M. E. (2006). The Maize Primary Cell Wall Mi-  
542 crofibril: A New Model Derived from Direct Visualization. **J. Agric. Food**  
543 **Chem.**, 54, 597–606.
- 544 Ding, S.-Y., Liu, Y.-S., Zeng, Y., Himmel, M. E., Baker, J. O., & Bayer,  
545 E. A. (2012). How Does Plant Cell Wall Nanoscale Architecture Correlate  
546 with Enzymatic Digestibility? **Science** 338, 1055–1060.
- 547 Ding, S.-Y., Zhao, S., & Zeng, Y. (2014). Size, shape, and arrangement of  
548 native cellulose fibrils in maize cell walls. **Cellulose** 21, 863–871.
- 549 Djahedi, C., hle Wohlert, M. B., Berglund, L. A., & Wohlert, J. (2016). Role  
550 of hydrogen bonding in cellulose deformation—the leverage effect analyzed  
551 by molecular modeling. **Cellulose** 23, 2315–2323.

- 552 Dufresne, A. (2017). *Nanocellulose. From Nature to High Performance Tai-*  
553 *lored Materials.* (2nd ed.). Berlin/Boston: Walter de Gruyter GmbH.
- 554 Elazzouzi-Hafraoui, S., Nishiyama, Y., Putaux, J.-L., Heux, L., Dubreuil,  
555 F., & Rochas, C. (2008). The shape and size distribution of crystalline  
556 nanoparticles prepared by acid hydrolysis of native cellulose. *Biomacromolecules*, 9, 57–65.
- 558 Eyley, S., & Thielemans, W. (2014). Surface modification of cellulose  
559 nanocrystals. *Nanoscale*, 6, 7764–7779.
- 560 French, A. D. (2017). Glucose, not cellobiose, is the repeating unit of cellulose  
561 and why that is important. *Cellulose*, 24, 4605–4609.
- 562 Gardebjer, S., Andersson, M., Engström, J., Restorp, P., Persson, M., &  
563 Larsson, A. (2016). Using Hansen solubility parameters to predict the  
564 dispersion of nano-particles in polymeric films. *Polym. Chem.*, 7, 1756–  
565 1764.
- 566 Habibi, Y., Lucia, L. A., & Rojas, O. J. (2010). Cellulose Nanocrystals:  
567 Chemistry, Self-Assembly, and Applications. *Chem. Rev.*, 110, 3479–3500.
- 568 Hamad, W. Y. (2017). *Cellulose Nanocrystals Properties, Production and*  
569 *Applications.* Chichester, U. K.: Wiley.
- 570 Hamad, W. Y., & Hu, T. Q. (2010). Structure-process-yield interrelation in  
571 nanocrystalline cellulose extraction. *Can. J. Chem. Eng.*, 88, 392–402.
- 572 Hansen, C. M. (1967a). The Three Dimensional Solubility Parameter - Key  
573 to Paint Component Affinities I. - Solvents, Plasticizers, Polymers, and  
574 Resins. *J. Paint Techn.*, 39, 104–117.
- 575 Hansen, C. M. (1967b). *The Three Dimensional Solubility Parameter and*  
576 *Solvent Diffusion Coefficient, Their Importance in Surface Coating For-*  
577 *mulation.* Ph.D. thesis Technical University of Denmark Copenhagen,  
578 Danemark.
- 579 Hansen, C. M. (1997). Cohesion Parameters for Surfaces, Pigments, and  
580 Fillers. *Surf. Coat. Int.*, 8, 386–391.
- 581 Hansen, C. M. (2007). *Hansen Solubility Parameters A User's Handbook.*  
582 Boca Raton, FL, U. S. A.: CRC Press.

- 583  
584                   *Holzforschung* 52
- 585  
586  
587                   *J. Paint Techn.* 39
- 588  
589  
590                   *Carbohydr. Res.* 306
- 591                   *The Solubility of Nonelectrolytes*
- 592
- 593                   *Regular Solutions*
- 594
- 595  
596  
597                   *Science* 315
- 598  
599  
600                   *Compos. Sci. Technol.* 154
- 601                   *Nature* 426
- 602  
603  
604                   *Biomacromolecules* 14
- 605  
606  
607                   *Powder Technol.* 261
- 608                   *Surface Chemistry of*
- 609                   *Surfactants and Polymers*
- 610  
611  
612                   *J. Microsc.-Oxford* 178

- 613 Larsson, A., & Johns, W. E. (1988). Acid-base interactions between cellulose/lignocellulose and organic molecules. *J. Adhesion*, 25, 121–131.
- 615 Lewandowska, A. E., & Eichhorn, S. J. (2016). Raman imaging as a tool for  
616 assessing the degree of mixing and the interface between polyethylene and  
617 cellulose nanocrystals. *IOP Conf. Ser. Mater. Sci. Eng.*, 139, 012030.
- 618 Li, Q., & Renneckar, S. (2011). Supramolecular Structure Characterization  
619 of Molecularly Thin Cellulose I Nanoparticles. *Biomacromolecules*, 12,  
620 650–659.
- 621 Liu, D., Chen, X., Y.Yue, Chen, M., & Wu, Q. (2011). Structure and rheology  
622 of nanocrystalline cellulose. *Carbohydr. Polym.*, 84, 311–322.
- 623 Machui, F., Langner, S., Zhu, X., Abbott, S., & Brabec, C. J. (2012). *Sol.  
Energ. Mat. Sol. C.*, 100, 138–146.
- 625 Marques, H. M. C. (2010). A review on cyclodextrin encapsulation of essential  
626 oils and volatiles. *Flavour Frag. J.*, 25, 313–326.
- 627 Matthews, J. F., Skopec, C. E., Mason, P. E., Zuccato, P., Torget, R. W.,  
628 Sugiyama, J., Himmel, H. E., & Brady, J. W. (2006). Computer simulation  
629 studies of microcrystalline cellulose I . *Carbohydr. Res.*, 341, 138–152.
- 630 Mazeau, K., & Rivet, A. (2008). Wetting the (110) and (100) Surfaces of I  
631 Cellulose Studied by Molecular Dynamics. *Biomacromolecules*, 9, 1352–  
632 1354.
- 633 Mazeau, K., & Wyszomirski, M. (2012). Modelling of Congo red adsorption  
634 on the hydrophobic surface of cellulose using molecular dynamics. *Cellulose*, 19, 1495–1506.
- 636 Medronho, B., Romano, A., Miguel, M. G., Stigsson, L., & Lindman, B.  
637 (2012). Rationalizing cellulose (in)solubility: reviewing basic physicochem-  
638 ical aspects and role of hydrophobic interactions. *Cellulose*, 19, 581–587.
- 639 Minhas, P. S., & Robertson, A. A. (1967). Accessibility of Cellulose by the  
640 Thallous Ethylate Method-Application to the Measurement of Cellulose  
641 Liquid Interactions 1. *Textile Res. J.*, 37, 400–408.

- 642 Moon, R. J., Martini, A., Nairn, J., Simonsen, J., & Youngblood, J. (2011).  
643 Cellulose nanomaterials review: structure, properties and nanocomposites.  
644 *Chem. Soc. Rev.* **40**, 3941–3994.
- 645 Nishiyama, Y. (2017). Molecular interactions in nanocellulose assembly. *Phil.  
646 Trans. R. Soc. A.* **376**, 20170047.
- 647 Nishiyama, Y., Langan, P., & Chanzy, H. (2002). Crystal Structure and  
648 Hydrogen-Bonding System in Cellulose I from Synchrotron X-ray and  
649 Neutron Fiber Diffraction. *J. Am. Chem. Soc.* **124**, 9074–9082.
- 650 Nishiyama, Y., Sugiyama, J., Chanzy, H., & Langan, P. (2003). Crystal  
651 Structure and Hydrogen Bonding System in Cellulose I from Synchrotron  
652 X-ray and Neutron Fiber Diffraction. *J. Am. Chem. Soc.* **125**, 14300–  
653 14306.
- 654 Peng, S. X., Chang, H., Kumar, S., Moon, R. J., & Youngblood, J. P. (2016).  
655 A comparative guide to controlled hydrophobization of cellulose nanocrystals  
656 via surface esterification. *Cellulose* **23**, 1825–1846.
- 657 Peng, S. X., Shrestha, S., Yoo, Y., & Youngblood, J. P. (2017). Enhanced  
658 dispersion and properties of a two-component epoxy nanocomposite using  
659 surface modified cellulose nanocrystals. *Polymer*, **112**, 359–368.
- 660 Petersson, L., Kvien, I., & Oksman, K. (2007). Structure and thermal proper-  
661 ties of poly(lactic acid)/cellulose whiskers nanocomposite materials. *Com-  
662 pos. Sci. Technol.* **67**, 2535–2544.
- 663 Raquez, J.-M., Habibi, Y., Murariu, M., & Dubois, P. (2013). Polylactide  
664 (PLA)-based nanocomposites. *Prog. Polym. Sci.* **38**, 1504–1542.
- 665 Reid, M. S., Villalobos, M., & Cranston, E. D. (2017). The role of hydro-  
666 gen bonding in non-ionic polymer adsorption to cellulose nanocrystals and  
667 silica colloids. *Curr. Opin. Colloid In.*, **29**, 76–82.
- 668 Sèbe, G., Ham-Pichavant, F., Ibarboure, E., Koffi, A. L. C., & Tingaut,  
669 P. (2012). Supramolecular Structure Characterization of Cellulose II  
670 Nanowhiskers Produced by Acid Hydrolysis of Cellulose I Substrates.  
671 *Biomacromolecules* **13**, 570–578.

- 672 Segal, L., Creely, J. J., Martin, Jr, A. E., & Conrad, C. M. (1959). An  
673 Empirical Method for Estimating the Degree of Crystallinity of Native  
674 Cellulose Using the X-Ray Diffractometer. *Text. Res.*, *29*, 786–794.
- 675 Siqueira, G., Bras, J., & Dufresne, A. (2010). New Process of Chemical Graft-  
676 ing of Cellulose Nanoparticles with a Long Chain Isocyanate. *Langmuir*,  
677 *26*, 402–411.
- 678 Sojoudiasli, H., Heuzey, M.-C., Carreau, P. J., & Riedl, B. (2017). Rheologi-  
679 cal behavior of suspensions of modified and unmodified cellulose nanocrys-  
680 tals in dimethyl sulfoxide. *Rheol. Acta*, *56*, 673–682.
- 681 Stefanis, E., & Panayiotou, C. (2008). Prediction of Hansen Solubility Pa-  
682 rameters with a New Group-Contribution Method. *Int. J. Thermophys.*,  
683 *29*, 568–585.
- 684 Uhlig, M., Fall, A., Wellert, S., Lehmann, M., Prévost, S., Wågberg, L.,  
685 von Klitzing, R., & Nyström, G. (2016). Two-dimensional aggregationand  
686 semidilute ordering in cellulose nanocrystals. *Langmuir*, *32*, 442–450.
- 687 Usov, I., Nyström, G., Adamcik, J., Handschin, S., Schütz, C., Fall, A.,  
688 Bergström, L., & Mezzenga, R. (2015). Understanding nanocellulose chi-  
689 rality and structureâ€¢properties relationship at the single fibril level. *Nat.*  
690 *Commun.*, *6*, 7564.
- 691 Wade, R. H., & Creely, J. J. (1974). Structure and Stability of Chloroform-  
692 Included Cotton Cellulose1. *Text. Res. J.*, *44*, 941–945.
- 693 Xu, X., Liu, F., Jiang, L., Zhu, J. Y., Haagenson, D., & Wiesenborn, D. P.  
694 (2013). Cellulose Nanocrystals vs. Cellulose Nanofibrils: A Compara-  
695 tive Study on Their Microstructures and Effects as Polymer Reinforcing  
696 Agents. *ACS Appl. Mater. Inter.*, *5*, 2999–3009.
- 697 Xu, X., Wang, H., Jiang, L., Wang, X., Payne, S. A., Zhu, J. Y., & Li, R.  
698 (2014). Comparison between Cellulose Nanocrystal and Cellulose Nanofib-  
699 ril Reinforced Poly(ethylene oxide) Nanofibers and Their Novel Shish-  
700 Kebab-Like Crystalline Structures. *Macromolecules*, *47*, 3409–3416.
- 701 Yamane, C., Aoyagi, T., Ago, M., Sato, K., Okajima, K., & Takahashi, T.  
702 (2006). Two different surface properties of regenerated cellulose due to  
703 structural anisotropy. *Polym. J.*, *38*, 819–826.

- 704 Yao, K., Meng, Q., Bulone, V., & Zhou, Q. (2017). Flexible and Respon-  
705 sive Chiral Nematic Cellulose Nanocrystal/Poly(ethylene glycol) Compos-  
706 ite Films with Uniform and Tunable Structural Color. *Adv. Mater.*, *29*,  
707 1701323.
- 708 Yin, Y., Tian, X., Jiang, X., Wang, H., & Gao, W. (2016). Modification  
709 of cellulose nanocrystal via SI-ATRP of styrene and the mechanism of its  
710 reinforcement of polymethylmethacrylate. *Carbohydr. Polym.*, *142*, 206  
711 212.
- 712 Yoo, Y., & Youngblood, J. P. (2016). Green One-Pot Synthesis of Surface  
713 Hydrophobized Cellulose Nanocrystals in Aqueous Medium *LCS Sustain-*  
714 *able Chem. Eng.*, *4*, 3927 3938.
- 715 Yu, H., & Qin, Z. (2012). Effect of Cellulose nanocrystal on Crystallization  
716 Behavior of Poly(3-hydroxybutyrate-co-3-hydroxyvalerate).  
717 *Adv. Mat. Res.*, *430-432*, 20 23.
- 718 Yu, H.-Y., Qin, Z.-Y., Liu, Y.-N., Chen, L., Liu, N., & Zhou, Z. (2012).  
719 Simultaneous improvement of mechanical properties and thermal stability  
720 of bacterial polyester by cellulose nanocrystals *Carbohydr. Polym.*, *89*,  
721 971 978.
- 722 Zhang, C., Salick, M. R., Cordie, T. M., Ellingham, T., Dan, Y., & Turng, L.-  
723 S. (2015). Incorporation of poly(ethylene glycol) grafted cellulose nanocrys-  
724 tals in poly(lactic acid) electrospun nanocomposite fibers as potential scaf-  
725 folds for bone tissue engineering *Mater. Sci. Eng. C Mater. Biol. Appl.*,  
726 *49*, 463 471.
- 727 Zhou, C., Chu, R., Wu, R., & Wu, Q. (2011). Electrospun polyethylene  
728 oxide/cellulose nanocrystal composite nanofibrous mats with homogeneous  
729 and heterogeneous microstructures *Biomacromolecules*, *12*, 2617 2625.